PEROVSKITES

Liquid-phase sintering of lead halide perovskites and metal-organic framework glasses

Jingwei Hou[1]*, Peng Chen[1,2], Atul Shukla[3,4], Andraž Krajnc[5], Tiesheng Wang[6], Xuemei Li[1], Rana Doasa[7], Luiz H. G. Tizei[8], Bun Chan[9], Duncan N. Johnstone[10], Rijia Lin[1], Tobias U. Schülli[11], Isaac Martens[11], Dominique Appadoo[12], Mark S' Ari[7], Zhiliang Wang[1,2], Tong Wei[13], Shih-Chun Lo[4,14], Mingyuan Lu[15], Shichun Li[16], Ebinazar B. Namdas[3,4], Gregor Mali[5], Anthony K. Cheetham[17,18], Sean M. Collins[19]*, Vicki Chen[1], Lianzhou Wang[1,2]*, Thomas D. Bennett[10]*

Lead halide perovskite (LHP) semiconductors show exceptional optoelectronic properties. Barriers for their applications, however, lie in their polymorphism, instability to polar solvents, phase segregation, and susceptibility to the leaching of lead ions. We report a family of scalable composites fabricated through liquid-phase sintering of LHPs and metal-organic framework glasses. The glass acts as a matrix for LHPs, effectively stabilizing nonequilibrium perovskite phases through interfacial interactions. These interactions also passivate LHP surface defects and impart bright, narrow-band photoluminescence with a wide gamut for creating white light-emitting diodes (LEDs). The processable composites show high stability against immersion in water and organic solvents as well as exposure to heat, light, air, and ambient humidity. These properties, together with their lead self-sequestration capability, can enable breakthrough applications for LHPs.

L ead halide perovskites (LHPs) exhibit tunable bandgaps, high charge carrier mobilities, and bright narrow-band photoluminescence (PL) that could offer advantages for optoelectronic applications over conventional silicon (Si)–based and binary II-VI, III-V, and IV-VI semiconducting materials (1). However, for successful tech-nological integration, LHPs must overcome their inherent polymorphism; decomposition upon exposure to polar solvents, oxygen, heat, and light; the presence of trap states; and the phase segregation and leaching of toxic heavy metal ions (2, 3). Targeted high optical absorptivity and direct band gaps optimal for photovoltaics and red-light light-emitting diode (LEDs), for example, are found in the $CsPbI_3$ pseudo-cubic "black" phases (α-, β-, and γ-phases), but thermodynamic factors promote their conversion to the inactive non-perovskite "yellow" δ-phase under ambient conditions (Fig. 1A) (4). LHP materials for white-light LEDs will critically depend on stabilization of this red emitter, ideally combined in a single broad-band luminescent material architecture.

The formation of LHP composites may offer solutions to some of these problems (5), but the ionic nature of LHPs is not entirely conducive to composite fabrication. Functional penalties incurred include LHP aggregation and decomposition, poor mechanical stability caused by weak interfacial interactions with the chosen matrix, and the formation of high concentrations of trap states (6). Research into a subfamily of metal-organic frameworks (MOFs) called zeolitic imidazolate frameworks (ZIFs) has enabled access to high-temperature ZIF liquids and microporous glasses after quenching (7). ZIF glasses have distinct physicochemical properties in terms of their porosity, reactivity, mechanical rigidity and ductility, and optical response (8–10) and have been used as host matrices for crystalline MOFs (11, 12). Together, these properties make ZIF glasses prime candidates for addressing the multiple challenges for LHP composite formation.

Fig. 1. Fabrication of $(CsPbI_3)_{0.25}(a_gZIF-62)_{0.75}$ composites at various sintering temperatures. (**A**) Phase transition of $CsPbI_3$ in its pure phase and within the composites. (**B**) Ex situ room-temperature synchrotron powder XRD for $(CsPbI_3)(a_gZIF-62)(25/75)$ (marked as Mixture) and $(CsPbI_3)_{0.25}(a_gZIF-62)_{0.75}$ composites fabricated with different sintering temperatures. cps, counts per second. (**C**) PL spectra and (**D**) ultraviolet-visible (UV-Vis) absorption spectra for $(CsPbI_3)_{0.25}(a_gZIF-62)_{0.75}$ composites fabricated at different sintering temperatures. Arrows indicate two band edges attributed to δ- and γ-$CsPbI_3$ observed for the sample prepared at 175°C. a.u., arbitrary units.
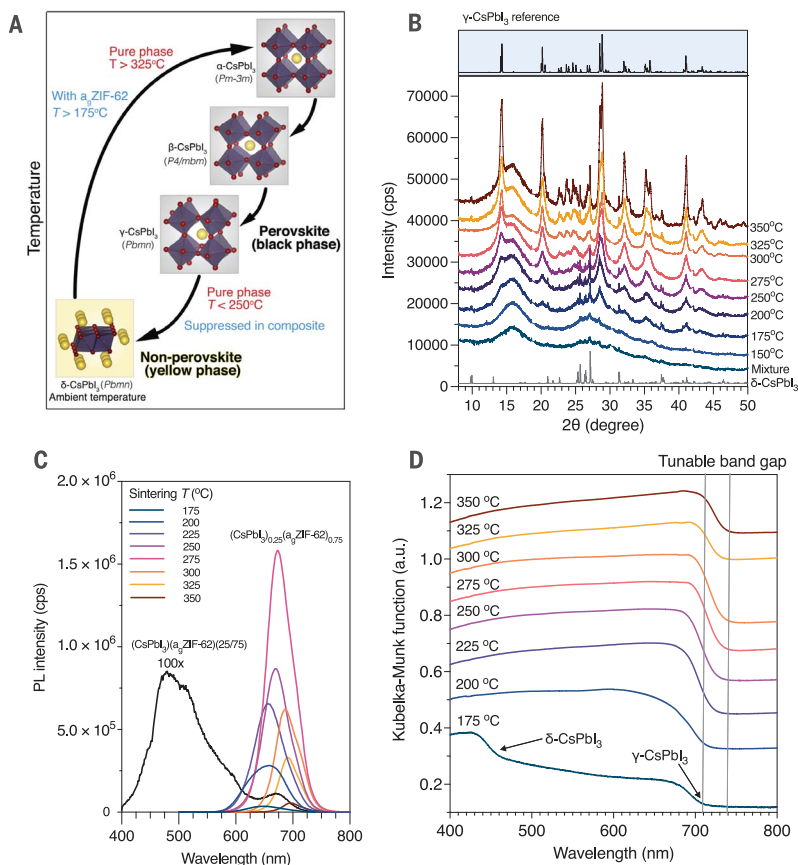
We describe a new class of composites, fabricated by means of liquid-phase sintering of crystalline LHPs and ZIF glass matrices, and show that industrial powder processing techniques used to form high-performance composites can be applied to chemically dissimilar LHPs and ZIF glasses. ZIF-62 {$Zn[(Im)_{1.95}(bIm)_{0.05}]$} (Im, imidazolate; bIm, benzimidazolate) and $CsPbI_3$ were first synthesized mechanochemically and showed the expected phase transitions (Fig. 1A and figs. S1 to S3) [13]. We then mixed 25 wt % $CsPbI_3$ with ZIF-62 glass [denoted as a_gZIF-62, glass transition temperature (T_g) ~ 304°C] (fig. S3B), and the mixtures are termed $(CsPbI_3)(a_gZIF$-62)(25/75) [11]. The ex situ synchrotron powder x-ray diffraction (XRD) pattern of $(CsPbI_3)(a_gZIF$-62)(25/75) (Fig. 1B, mixture pattern) exhibited weak Bragg peaks, ascribed to the nonperovskite δ-$CsPbI_3$ phase. The mixture was sintered at different temperatures (up to 350°C) and then quenched with liquid nitrogen (referred to as cryogenic quenching) under flowing argon (Ar). The resultant composites, called $(CsPbI_3)_{0.25}(a_gZIF$-62)$_{0.75}$, showed XRD features consistent with the metastable γ-$CsPbI_3$ phase, with gradually increasing intensity with higher sintering temperatures (Fig. 1B and fig. S4). Negligible weight loss was observed during sintering (fig. S5).

The broad PL emission of a_gZIF-62 was reduced after mixing with $CsPbI_3$, which we attribute to photon absorption by $CsPbI_3$ (fig. S6) [14]. The $(CsPbI_3)_{0.25}(a_gZIF$-62)$_{0.75}$ composites started to show red PL emission after sintering-quenching at 175°C, with the strongest PL obtained with 275°C (Fig. 1C). Higher sintering temperatures red-shifted the PL maxima (fig. S7), which was concomitant with an observed decrease in the optical band gaps (Fig. 1D and fig. S6C). They also led to a lower defect density and enhanced homogeneity for the $CsPbI_3$ component, as indicated by the reduced PL full-widths at half-maximum (FWHM) and the
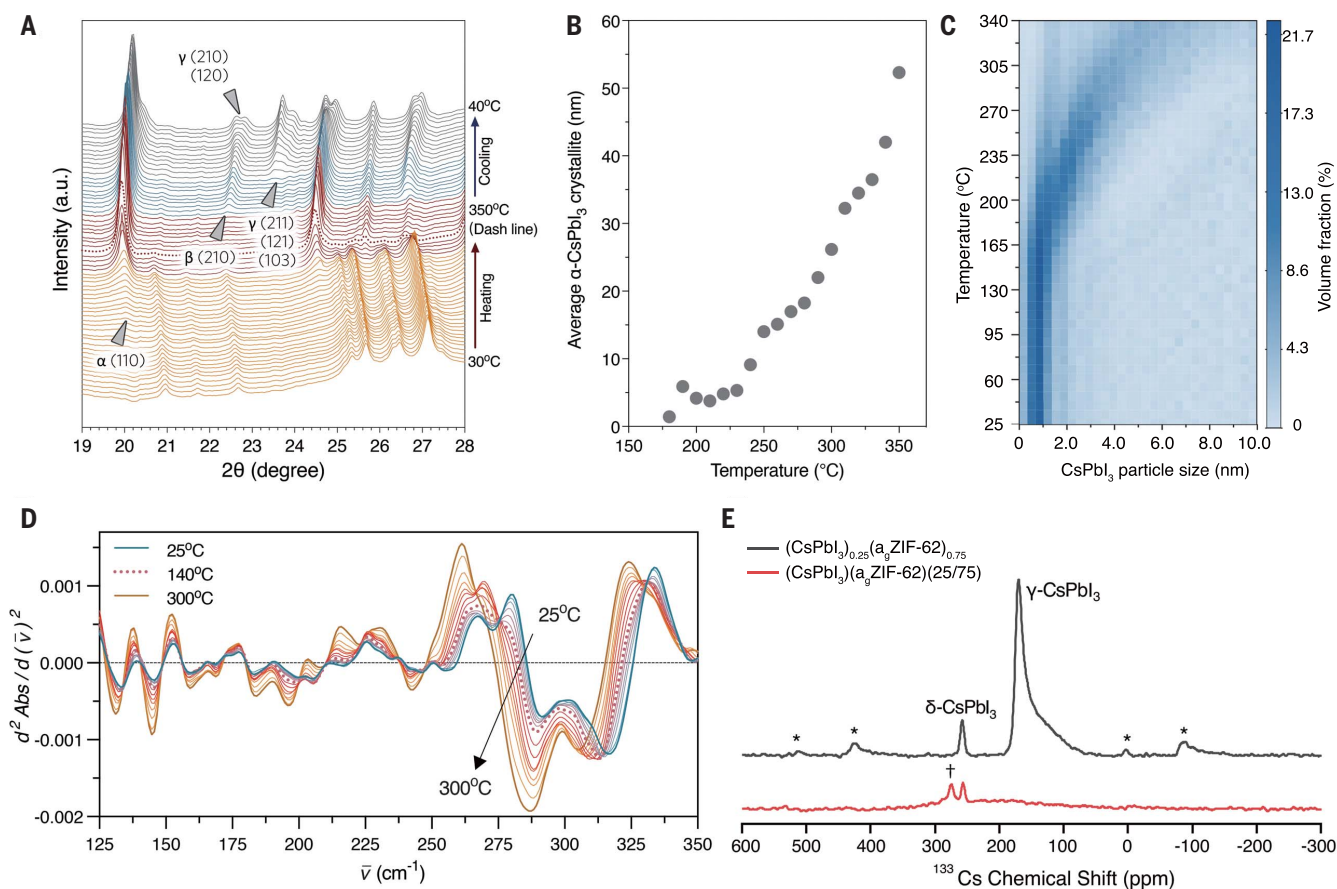

Fig. 2. Structure and bonding evolution during sintering. (**A**) Temperature-resolved, high-resolution in situ synchrotron powder XRD for $(CsPbI_3)(a_gZIF$-62)(25/75), with the Bragg peak *hkl* indices marked for different $CsPbI_3$ phases. The dominating phases are color-coded as δ, yellow; α, red; β, blue; and γ, gray. (**B**) Average sizes of α-$CsPbI_3$ deconvoluted from in situ powder XRD. (**C**) $CsPbI_3$ particle-size evolution during sintering fitted from in situ SAXS patterns. (**D**) Temperature-resolved second-derivative in situ THz FarIR spectra for $(CsPbI_3)(a_gZIF$-62)(25/75) during the first heating ramp. (**E**) ^{133}Cs MAS NMR spectra of $(CsPbI_3)(a_gZIF$-62)(25/75) and 275°C sintered $(CsPbI_3)_{0.25}(a_gZIF$-62)$_{0.75}$. Asterisks indicate spinning sidebands, and dagger symbol (†) indicates the weak signal of CsI.

[1]School of Chemical Engineering, The University of Queensland, St Lucia, QLD, 4072 Australia. [2]Australian Institute for Bioengineering and Nanotechnology, The University of Queensland, St Lucia, QLD, 4072 Australia. [3]School of Mathematics and Physics, The University of Queensland, St Lucia, QLD, 4072 Australia. [4]Centre for Organic Photonics and Electronics, The University of Queensland, Brisbane, QLD 4072, Australia. [5]Department of Inorganic Chemistry and Technology, National Institute of Chemistry, 1001 Ljubljana, Slovenia. [6]School of Mechanical Engineering, Shanghai Jiao Tong University, Shanghai 200240, China. [7]School of Chemical and Process Engineering, University of Leeds, Leeds LS2 9JT, UK. [8]Université Paris-Saclay, CNRS, Laboratoire de Physique des Solides, 91405, Orsay, France. [9]Graduate School of Engineering, Nagasaki University, Nagasaki 852-8521 Japan. [10]Department of Materials Science and Metallurgy, University of Cambridge, Cambridge, CB3 0FS, UK. [11]The European Synchrotron Radiation Facility (ESRF), 38000 Grenoble, France. [12]Australian Synchrotron, Clayton, VIC, 3168 Australia. [13]College of Science, Civil Aviation University of China, Tianjin 300300, China. [14]School of Chemistry and Molecular Biosciences, The University of Queensland, St Lucia, QLD, 4072 Australia. [15]School of Mechanical and Mining Engineering, The University of Queensland, St Lucia, QLD, 4072 Australia. [16]Institute of Chemical Materials, China Academy of Engineering Physics, Mianyang 621900, China. [17]Materials Research Laboratory, University of California, Santa Barbara, CA 93106, USA. [18]Department of Materials Science and Engineering, National University of Singapore, Singapore, 117576 Singapore. [19]School of Chemical and Process Engineering and School of Chemistry, University of Leeds, Leeds LS2 9JT, UK.
*Corresponding author. Email: jingwei.hou@uq.edu.au (J.H.); s.m.collins@leeds.ac.uk (S.M.C.); l.wang@uq.edu.au (L.W.); tdb35@cam.ac.uk (T.D.B.)

longer excited-state lifetimes (fig. S8 and table S1) (15). Compared with a slower quenching, rapid cryogenic quenching formed materials with optimal PL lifetimes and PL quantum yields (PLQYs) (>50%) (figs. S9 and S10 and table S1).

Temperature-resolved high-resolution in situ synchrotron powder XRD was collected for $(CsPbI_3)(a_gZIF-62)(25/75)$ (Fig. 2A and fig. S11). The emerging peaks from ~170°C indicate the formation of α-$CsPbI_3$ ($Pm\text{-}3m$). These peaks intensified at higher sintering temperatures. During the quenching stage, the gradual emergence of β-$CsPbI_3$ ($P4/mbm$) (from ~250°C) and γ-$CsPbI_3$ ($Pbnm$) (from ~150°C) was evidenced (16). The deconvoluted α-$CsPbI_3$ crystallite size increased during sintering (Fig. 2B), which is consistent with the changes in band gap caused by quantum-confinement effects (5).

The evolution of α-$CsPbI_3$ crystallite size can be attributed to coarsening of $CsPbI_3$ grains and the phase transition from bulkier δ-$CsPbI_3$ crystallites, a cascade confirmed with synchrotron in situ small-angle x-ray scattering (SAXS). Coarsening of $CsPbI_3$ grains mainly occurred in the size range smaller than the XRD deconvoluted crystallite size at <10 nm, starting from 165°C (Fig. 2C and figs. S12 to S14). Upon sintering, atoms in $CsPbI_3$ grains became mobile from the Tamman temperature (T_{Tamman} ~ 103°C) as approximated by 0.5 T_{melt} (melt temperature) in degrees kelvin (16, 17). A similar response could also be expected for a_gZIF-62. Characteristic of liquid-phase sintering, $CsPbI_3$ grain coarsening and composite densification were observed at a temperature lower than the inherent T_g of a_gZIF-62 (~304°C) (fig. S15) (18).

The emergence of an interface resulting from densification occurs analogously to surface energy–controlled transitions from δ- to α-phase in solvent-modulated or ligand-capped $CsPbI_3$ quantum dots (19, 20), with the interfacial energy dominant for smaller grains resulting in phase transitions at lower temperatures. To examine our hypothesis that intimate interfacial contact is critical for phase control, we synthesized $[Zn(Im)_{1.75}(bIm)_{0.25}]$ a_gZIF-62 with a higher T_{melt} and higher viscosity caused by bulkier bIm ligands and subsequently demonstrated the expected higher residual δ-$CsPbI_3$ content in the composite (fig. S16).

We further probed the changes in interfacial bonding within $(CsPbI_3)_{0.25}(a_gZIF\text{-}62)_{0.75}$ by means of temperature-resolved synchrotron terahertz (THz) radiation and far-infrared (FarIR)
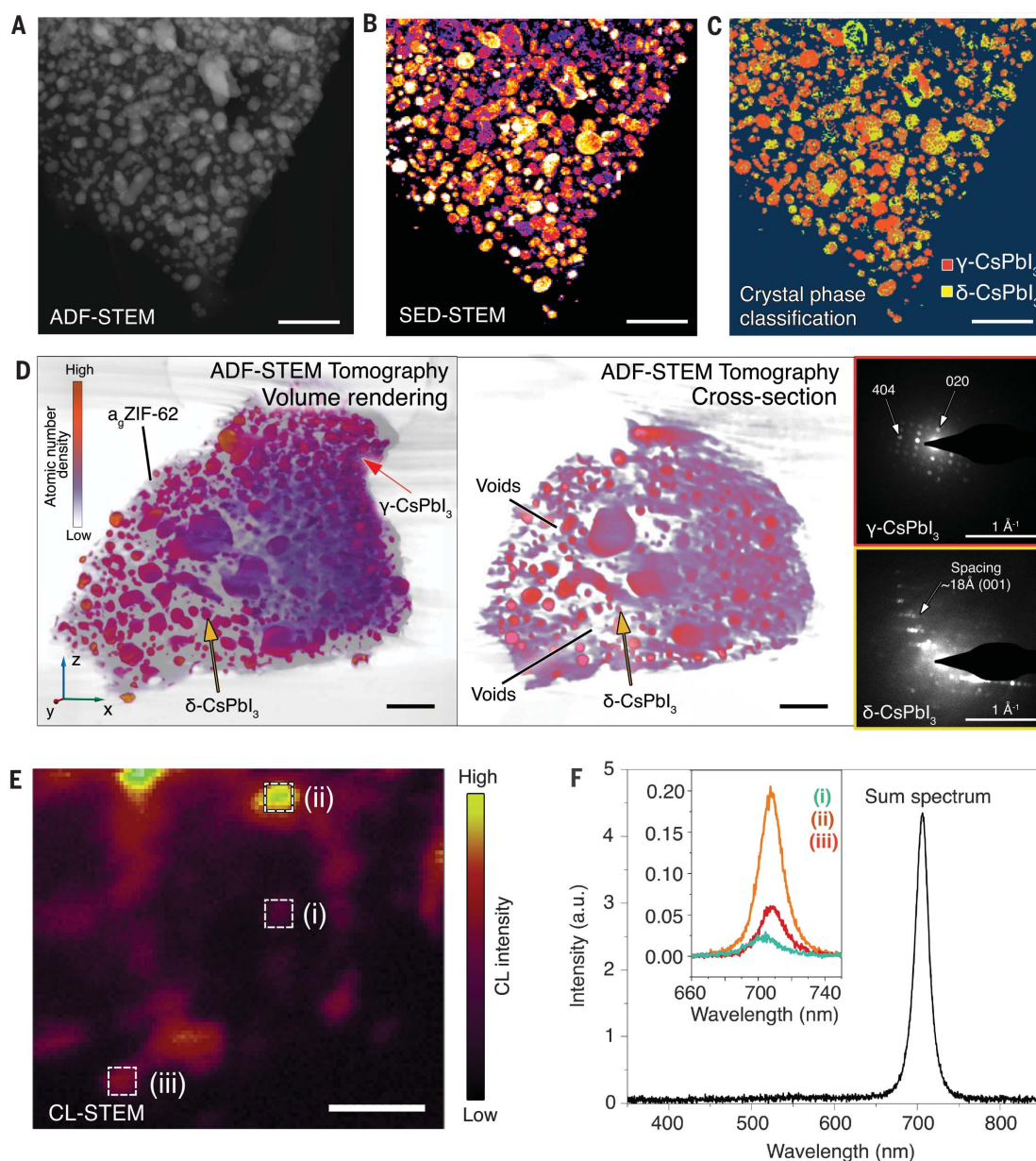

Fig. 3. Phase distribution for the $(CsPbI_3)_{0.25}(a_gZIF\text{-}62)_{0.75}$ composite fabricated with 300°C sintering. (**A**) ADF-STEM image, (**B**) SED-STEM mapping, and (**C**) $CsPbI_3$ crystal phase classification results for $(CsPbI_3)_{0.25}(a_gZIF\text{-}62)_{0.75}$ composite. (**D**) Volume rendering of a tomographic reconstruction of $(CsPbI_3)_{0.25}(a_gZIF\text{-}62)_{0.75}$ and a single cross-sectional plane extracted from the volume. Color-coded arrows indicate the regions where electron diffraction data were collected. Scale bars, (A) to (D) 250 nm. (**E**) CL-STEM mapping of the integrated CL intensity. Scale bar, 70 nm. (**F**) CL spectra acquired at each STEM probe position. (Inset) The sum CL spectrum of the whole region in (E).
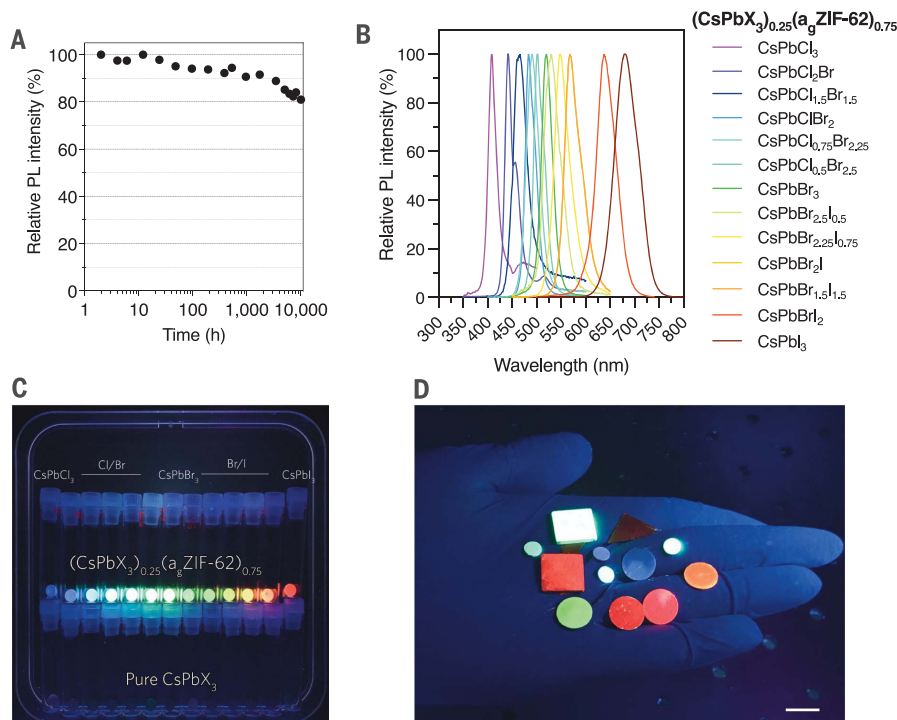
Fig. 4. Stability and optical performance of the composites. (**A**) Change of the relative PL intensity for $(CsPbI_3)_{0.25}(a_gZIF-62)_{0.75}$ immersed in the Milli-Q water. Sample was sintered at 300°C. (**B**) Normalized PL intensities of the $(CsPbX_3)_{0.25}(a_gZIF-62)_{0.75}$ composites (X = Cl, Br, I, and mixed halide ions). (**C** and **D**) Optical photos of the composites and pure $CsPbX_3$ under 365 nm UV light. Composites for (B) to (D) were sintered at 275°C. Scale bar, 1 cm.

vibrational spectroscopy. The second-derivative spectra revealed the fine vibrational modes of Zn tetrahedra (Fig. 2D and figs. S17 and S18) (9). The modes assigned to Zn-N vibrations (~287 cm^{-1}) and Zn-I stretching (~135 cm^{-1}) within $Zn(Im)_2(bIm)I$ tetrahedra through density functional theory (fig. S19) began to intensify with increasing temperature from ~140°C. These changes were consistent with the endothermic response at ~140°C in the first heating ramp of differential scanning calorimetry (DSC) measurements, which was concomitant with changes in $CsPbI_3$ binding observed in phonon signatures and in ex situ spectroscopy (figs. S20 to S23).

Magic-angle–spinning nuclear magnetic resonance (MAS NMR) spectroscopy provided insights into the different species complementary to vibrational spectroscopy. The broader signals from composite ^{13}C and ^{15}N spectra indicated additional disorder of ZIF component over the powder mixture (fig. S24). The ^{133}Cs MAS NMR spectra of $(CsPbI_3)(a_gZIF-62)(25/75)$ exhibited narrow signals of δ-$CsPbI_3$ [260 parts per million (ppm)] (21) and CsI (~280 ppm). Broad, low signals extending between 0 and ~350 ppm can be ascribed to poorly crystalline, highly defective $CsPbI_3$ (Fig. 2E and fig. S25). After sintering, the broad contributions and CsI peaks diminished, and the major signals stemmed from γ-$CsPbI_3$. These signals exhibited notable shoulders (160 to 80 ppm), with

shoulder intensities highly dependent on the sintering conditions. They could be assigned to Cs nuclei on or near the surface of $CsPbI_3$ grains where structural defects, sites of the interaction between the γ-$CsPbI_3$ and $a_gZIF-62$, or both are abundant. Also, the signals of the δ-$CsPbI_3$ of the same sample exhibited no shoulder, which is consistent with less interfacial contact between δ-$CsPbI_3$ and $a_gZIF-62$.

These observations allowed us to propose a mechanism for γ-$CsPbI_3$ stabilization within composites (22, 23). The α-, β-, and γ-phases of $CsPbI_3$ have double-well phonon modes at the center of the Brillouin zone, driving the phase transition to δ-$CsPbI_3$ in a concerted phonon manner (24). The interfacial bonding disrupts the local Pb-I sublattice phonon modes and therefore avoids the harmonic order-disorder entropy (25, 26). Together with the physical confinement effect offered by the matrices, these factors counter the strong thermodynamic driving force to form δ-$CsPbI_3$.

We evaluated this mechanism further and verified embedded nanocrystals of γ-$CsPbI_3$ as the source of luminescence using microscopic measurements. After sintering, the mixture of particles became a monolith, with a smooth surface observed in scanning electron microscopy (SEM) (figs. S26 and S27). Annular dark-field scanning transmission electron microscopy (ADF-STEM) of $(CsPbI_3)_{0.25}(a_gZIF-62)_{0.75}$ showed pronounced atomic number contrast between

the two phases, which was further corroborated with energy-dispersive x-ray spectroscopy (STEM-EDS) elemental distribution mapping (Fig. 3A and fig. S28). The crystalline and amorphous regions were identified by means of scanning electron diffraction (SED) (27), with regions exhibiting Bragg diffraction corresponding to crystalline $CsPbI_3$ grains (Fig. 3B). Convolutional neural network (CNN) classification identified γ-$CsPbI_3$ as the major phase within the composite fragment. Individual grains were single-crystalline, whereas the speckle in the classification map arose from inherent ambiguities because of overlap in the diffraction peaks expected from δ- and γ-$CsPbI_3$ (Fig. 3C and figs. S29 and S30). The average size of $CsPbI_3$ from STEM was ~30 nm (fig. S31), readily modulated by extended ball milling before sintering, which further enhanced the composite PLQY to >65% because of a more pronounced quantum confinement effect (fig. S32) (5).

To probe the internal structure, we performed ADF-STEM tomography on a shard (>1 μm) of $(CsPbI_3)_{0.25}(a_gZIF-62)_{0.75}$ (Fig. 3D). The voids in cross sections of the volume are characteristic of densification processes in liquid phase sintering (18). Point diffraction data identified both δ-$CsPbI_3$ and γ-$CsPbI_3$ within the particle. A high degree of interfacial contact was correlated with γ-$CsPbI_3$, which is consistent with the hypothesized phase control through interfacial stabilization (fig. S33). STEM-based cathodoluminescence (CL) detected strong, narrow luminescence from isolated grains (<40 nm), with minor interparticle emission wavelength shifts (Fig. 3, E and F, and fig. S34). The variation of CL intensity is complex in origin, highly sensitive to the crystal quality and exposure to unpassivated surface states and particle size effects (28). Despite this, the CL spectra from individual grains provided incontrovertible evidence of luminescence from glass-bound nanocrystals of γ-$CsPbI_3$.

Returning to the aim of achieving long device lifetimes, we evaluated the composites in diverse environmental and operational settings. The rigid, hydrophobic $a_gZIF-62$ provided protection for $CsPbI_3$ (figs. S35 and S36), leading to stable PL emission for $(CsPbI_3)_{0.25}(a_gZIF-62)_{0.75}$ after extended (~20 hours) sonication in various nonpolar, polar protic, and polar aprotic organic solvents (fig. S37). The composite also exhibited stability against 10,000 hours immersion in water, storage under ambient conditions for 650 days, mild heating, and continuous laser excitation (~57 mW/cm^2) for >5000 s (Fig. 4A and figs. S38 to S40). The microporous composite design presents a key route to sequestration of toxic components (figs. S41 and S42), or to potential photochemical platforms where the $CsPbI_3$ crystals are not electronically insulated (fig. S43). $(CsPbI_3)_{0.25}(a_gZIF-62)_{0.75}$ made from mechanochemical precursors have similar performance compared with

the solvothermal precursors, making the composite promising for up-scaling (fig. S44). Collectively, $(CsPbI_3)_{0.25}(a_gZIF-62)_{0.75}$ offers substantial advantages over LHP composites with other substrates (fig. S45 and table S2).

Last, an array of composites were formed from $CsPbX_3$ (X = Cl, Br, and mixed halide ions) and $a_gZIF-62$, showing a wide color gamut with narrow PL peaks (Fig. 4, B and C, and table S3). For all the $CsPbX_3$ composites, their absolute PL intensities were at least two orders of magnitude higher than those of the corresponding pure $CsPbX_3$ samples, either as synthesized or after being treated with identical sintering (fig. S46). These properties, together with the high processibility (Fig. 4D), render these monolithic materials ideal candidates for downshifting white LEDs (fig. S47).

REFERENCES AND NOTES

1. M. V. Kovalenko, L. Protesescu, M. I. Bodnarchuk, *Science* **358**, 745–750 (2017).
2. X. Li *et al.*, *Nature* **578**, 555–558 (2020).
3. T. A. S. Doherty *et al.*, *Nature* **580**, 360–366 (2020).
4. Y. Wang *et al.*, *Science* **365**, 591–595 (2019).
5. J. Shamsi, A. S. Urban, M. Imran, L. De Trizio, L. Manna, *Chem. Rev.* **119**, 3296–3348 (2019).
6. Q. A. Akkerman, G. Rainò, M. V. Kovalenko, L. Manna, *Nat. Mater.* **17**, 394–405 (2018).
7. T. D. Bennett *et al.*, *J. Am. Chem. Soc.* **138**, 3484–3492 (2016).
8. R. S. K. Madsen *et al.*, *Science* **367**, 1473–1476 (2020).
9. J. Hou *et al.*, *J. Am. Chem. Soc.* **142**, 3880–3890 (2020).
10. L. Frentzel-Beyme, M. Kloß, P. Kolodzeiski, R. Pallach, S. Henke, *J. Am. Chem. Soc.* **141**, 12362–12371 (2019).
11. J. Hou *et al.*, *Nat. Commun.* **10**, 2580 (2019).
12. C. W. Ashling *et al.*, *J. Am. Chem. Soc.* **141**, 15641–15648 (2019).
13. J. A. Steele *et al.*, *Science* **365**, 679–684 (2019).
14. N. J. L. K. Davis *et al.*, *J. Phys. Chem. C Nanometer Interfaces* **121**, 3790–3796 (2017).
15. K. M. Boopathi *et al.*, *ACS Energy Lett.* **5**, 642–649 (2020).
16. A. Marronnier *et al.*, *ACS Nano* **12**, 3477–3486 (2018).
17. Y. Dai, P. Lu, Z. Cao, C. T. Campbell, Y. Xia, *Chem. Soc. Rev.* **47**, 4314–4331 (2018).
18. R. M. German, P. Suri, S. J. Park, *J. Mater. Sci.* **44**, 1–39 (2009).
19. Y. Wang *et al.*, *Adv. Mater.* **32**, e2000186 (2020).
20. B. Zhao *et al.*, *J. Am. Chem. Soc.* **140**, 11716–11725 (2018).
21. A. Karmakar *et al.*, *Chem. Commun.* **55**, 5079–5082 (2019).
22. R. Wang *et al.*, *Science* **366**, 1509–1513 (2019).
23. S. Bai *et al.*, *Nature* **571**, 245–250 (2019).
24. A. Marronnier *et al.*, *J. Phys. Chem. Lett.* **8**, 2659–2665 (2017).
25. M. Grechko, S. A. Bretschneider, L. Vietze, H. Kim, M. Bonn, *Angew. Chem. Int. Ed.* **57**, 13657–13661 (2018).
26. B. Wang, N. Novendra, A. Navrotsky, *J. Am. Chem. Soc.* **141**, 14501–14504 (2019).
27. O. Panova *et al.*, *Micron* **88**, 30–36 (2016).
28. J. T. Griffiths *et al.*, *ACS Appl. Energy Mater.* **2**, 6998–7004 (2019).

Science

Liquid-phase sintering of lead halide perovskites and metal-organic framework glasses

Jingwei HouPeng ChenAtul ShuklaAndraž KrajncTiesheng WangXuemei LiRana DoasaLuiz H. G. TizeiBun ChanDuncan N. JohnstoneRijia LinTobias U. SchülliIsaac MartensDominique AppadooMark S' AriZhiliang WangTong WeiShih-Chun LoMingyuan LuShichun LiEbinazar B. NamdasGregor MaliAnthony K. CheethamSean M. CollinsVicki ChenLianzhou WangThomas D. Bennett

Stable emission in glass

Lead halide perovskites can exhibit bright, narrow band photoluminescence but have stability issues related to formation of inactive phases and the loss of lead ions. Hou *et al.* show that the black, photoactive phase of cesium lead iodide can be stabilized by forming a composite with a glassy phase of a metal-organic framework through liquid-phase sintering. The photoluminescence is at least two orders of magnitude greater than that of the pure perovskite. The glass stabilizes the perovskite under high laser excitation, and about 80% of the photoluminescence was maintained after 10,000 hours of water immersion. —PDS

View the article online
https://www.science.org/doi/10.1126/science.abf4460
Permissions
https://www.science.org/help/reprints-and-permissions

Use of this article is subject to the Terms of service